Research Article

Journal of Environmental Nanotechnology

Development of PANI/TiO_2 Nanocomposites for Visible-light-driven Photocatalytic Treatment of Dye-contaminated Wastewater

Vijay R Khawale[1], P. Satishkumar[2*], Sugumari Vallinayagam[3], Manoj Tripathi[4], Anju Rani[5], M. Harish[6] and Barun Haldar[7]

[1]Department of Mechanical Engineering, Yeshwantrao Chavan College of Engineering, Nagpur, MH, India
[2]Department of Mechanical Engineering, Rathinam Technical Campus, Coimbatore, TN, India
[3]Department of Biotechnology, Vel Tech Rangarajan Dr. Sagunthala R&D Institute of Science and Technology, Avadi, Chennai, TN, India
[4]Department of Physics and Materials Science and Engineering, Jaypee Institute of Information Technology, A-10, Sector 62, Noida, UP, India
[5]Department of Physics, School of Engineering and Technology, CGC University, Mohali, PB, India
[6]Department of Aeronautical Engineering, Hindusthan Institute of Technology, Coimbatore, TN, India
[7]Department of Industrial Engineering, College of Engineering, Imam Mohammad Ibn Saud Islamic University (IMSIU), Riyadh, Saudi Arabia
Received: 23.06.2026 Accepted: 27.07.2026 Published: xx.xx.xxxx
*spsatishkumar1986@gmail.com

ABSTRACT

The limited visible-light response of TiO_2 and the rapid recombination of its photogenerated charge carriers restrict its practical application in solar wastewater treatment. Although TiO_2-based composites have been widely investigated, comparative studies evaluating PANI/TiO_2 against multiple chemically distinct dyes under natural sunlight remain limited. In this study, PANI, TiO_2 nanoparticles, and a PANI/TiO_2 nanocomposite were synthesized and characterized using FTIR, UV-visible spectroscopy, and XRD. The novelty of the work lies in integrating the visible-light-harvesting and charge-transport properties of PANI with the photocatalytic stability of TiO_2 and evaluating the resulting composite against methylene blue, malachite green, and Bismarck brown under natural sunlight. The PANI/TiO_2 nanocomposite exhibited substantially greater photocatalytic activity than the individual materials, achieving up to 98% dye degradation under the tested conditions. This enhancement is attributed to improved solar-light absorption and interfacial charge transfer, which reduce electron-hole recombination. The use of natural sunlight eliminates the need for energy-intensive artificial irradiation, highlighting the potential of PANI/TiO_2 as a low-energy photocatalyst for the treatment of dye-contaminated water.

Keywords: Methylene blue; Nanocomposite; Photocatalytic activity; Malachite green; Nanoparticle synthesis.

1. INTRODUCTION

The increasing discharge of industrial effluents into natural water bodies has become a serious worldwide environmental challenge. Among various pollutants, synthetic organic contaminants are of particular concern because of toxicity, persistence, and resistance to natural degradation processes (Loganathan *et al.* 2026). The accumulation of these pollutants adversely affects aquatic ecosystems and poses potential risks to human health (Patidar *et al.* 2026). Therefore, the development of efficient, cost-effective, and environmentally sustainable remediation technologies has become an important area of research (Gaddala *et al.* 2025). Advanced treatment approaches capable of effectively removing organic pollutants from wastewater are highly desirable for ensuring environmental protection and water quality preservation. Synthetic dyes from industrial effluents are major water pollutants that threaten aquatic ecosystems (Rao *et al.* 2025). TiO_2 has been widely studied as a photocatalyst due to its strong oxidation ability, stability, and low cost. TiO_2 layers have shown effective dye degradation, making them promising materials for wastewater treatment (Kisała *et al.* 2021). TiO_2-impregnated montmorillonite clay photocatalysts have demonstrated effective photocatalytic degradation of MB, with the TiO_2/K-10 catalyst achieving more than 98% dye removal owing to high surface area and enhanced TiO_2 dispersion. These findings highlight the importance of support materials in improving photocatalytic performance for wastewater treatment applications (Rigoti *et al.* 2019). FTIR characterization confirmed the formation of Cu-doped TiO_2 photocatalysts, which exhibited enhanced photocatalytic activity and complete degradation of 10 mg/L gabapentin within 20 min under UVA-LED irradiation (Ahmadiasl *et al.* 2022).

Iron-doped TiO_2 bio-nanocomposites were developed to improve visible-light-driven photocatalytic activity. The incorporation of iron nanoparticles reduced the band-gap energy and improved light absorption. Moreover, enhanced electron–hole separation contributed to improved photocatalytic performance

(Chkirida *et al.* 2020). XRD analysis confirmed the successful formation of TiO_2/NiO composites, where synergistic interactions between TiO_2 and NiO enhanced photocatalytic activity, achieving 95.78% methylene blue degradation under sunlight irradiation (Weldekirstos *et al.* 2025). Ca–N co-doped TiO_2 photocatalysts demonstrated enhanced visible-light-driven methylene blue degradation following pseudo-first-order kinetics, highlighting the beneficial role of co-doping in improving photocatalytic performance (Abedin *et al.* 2026). Characterization studies confirmed the successful formation of modified TiO_2 nanocomposites, where the incorporation of N, S-CQDs and mesoporous carbon supports enhanced visible-light absorption, improved catalyst dispersion, and promoted synergistic interactions, thereby resulting in superior photocatalytic performance under visible-light irradiation (Koe *et al.* 2020).

TiO_2/SBA-16 mesoporous composites were successfully synthesized via a one-pot method and exhibited a well-ordered porous structure with high surface area, where incorporation of TiO_2 improved photocatalytic activity through improved dispersion and active site availability, achieving up to ~90% phenol degradation for efficient organic pollutant removal (Gholizadeh *et al.* 2020). SEM analysis confirmed the successful formation of polyaniline-coated graphene–TiO_2 nanocomposites, which exhibited enhanced visible-light-driven photocatalytic degradation of methyl orange, demonstrating the potential of PANI-based TiO_2 systems for wastewater remediation. (Gunti *et al.* 2017). The enhanced visible-light response observed for g-C_3N_4/PANI-modified TiO_2 nanotube arrays was attributed to improved light harvesting and rapid charge separation, resulting in superior catalytic performance (Zhou *et al.* 2020).

A γ-Fe_2O_3@PANI@TiO_2 heterojunction photocatalyst exhibited enhanced light utilization, excellent stability, and improved photocatalytic oxidation performance, demonstrating the beneficial role of PANI in promoting charge separation and photocatalytic activity (Wang *et al.* 2020). PANI@NiO composites were successfully synthesized via in-situ polymerization and exhibited enhanced photocatalytic activity toward Rhodamine B degradation. The improved performance was attributed to the synergistic interaction between PANI and NiO, which facilitated charge transfer and photocatalytic reactions (Usman *et al.* 2020). PANI/g-C_3N_4/Cr_2O_3 ternary composites exhibited enhanced photocatalytic activity due to synergistic interfacial interactions and reduced electron–hole recombination, highlighting the effectiveness of multi-component conducting polymer heterojunctions for pollutant degradation (Hiremath *et al.* 2025).

The incorporation of PANI and Ag nanoparticles into a g-C_3N_4 matrix enhanced visible-light absorption and promoted efficient photogenerated electron transport, demonstrating the potential of ternary photocatalytic systems for dye degradation under visible-light irradiation (Vivek *et al.* 2026; Hema et al. 2025; Chinnusamy, 2024). PANI nanofibers achieved 97% degradation of methyl orange within 3 h and followed pseudo-first-order kinetics with a rate constant of 0.0505 g mg^{-1} min^{-1}, demonstrating the photocatalytic potential of conducting polymers (Saha *et al.* 2020). V_2O_5–TiO_2 nanohybrid synthesized via sonication exhibited efficient photocatalytic decolorization of Congo red under pseudo-first-order kinetics, achieving ~96% degradation with a rate constant of 0.03567 min^{-1}, demonstrating its high potential for wastewater treatment applications (Idriss *et al.* 2023). TiO_2/g-C_3N_4 composite photocatalysts have demonstrated enhanced dye degradation performance owing to improved charge-transfer characteristics, reactive oxygen species generation, and favorable photocatalytic kinetics, highlighting the effectiveness of TiO_2-based hybrid systems for wastewater treatment (Hassan *et al.* 2022). TiO_2/XG photocatalysts exhibited efficient solar-driven degradation of reactive dyes following Langmuir–Hinshelwood pseudo-first-order kinetics, demonstrating the potential of immobilized TiO_2 systems for wastewater treatment applications (Alwared *et al.* 2023).

TiO_2/ZnO nanocomposites prepared via sol–gel method exhibited enhanced visible-light absorption due to semiconductor coupling, achieving ~95.11% photodegradation of thiazine dye under sunlight, while also showing stable performance over five reuse cycles, indicating excellent photocatalytic durability (Jebasingh *et al.* 2024). Cr_2S_3–GO/TiO_2 ternary composites exhibited high photocatalytic efficiency toward methylene blue (98.3%), rhodamine B (96.6%), and methyl orange (86.3%) degradation under visible light, attributed to enhanced visible-light utilization and defect-mediated interfacial interactions (Hasan *et al.* 2020). PANI/MIL-88A(Fe) composites exhibited enhanced photocatalytic behavior owing to improved conductivity and efficient photogenerated electron–hole separation, while also demonstrating excellent stability and recyclability (Chen *et al.* 2020).

Unlike previously reported complex or ternary PANI/TiO_2-based systems, the present study investigates a simple binary PANI/TiO_2 nanocomposite and directly compares it with pristine PANI and TiO_2 for the degradation of three chemically different dyes—methylene blue, malachite green, and Bismarck brown—under natural sunlight. PANI was selected because of its strong visible-light absorption, electrical conductivity, environmental stability, low cost, and facile synthesis. Under visible-light irradiation, photoexcited electrons from PANI can be transferred to TiO_2, while the resulting holes remain on PANI. This interfacial charge transfer may suppress electron–hole recombination and promote the formation of reactive species responsible for dye

degradation. Thus, the novelty of this study lies in the comparative evaluation of a simple PANI/TiO_2 nanocomposite for multi-dye removal using natural solar irradiation, demonstrating its potential for energy-efficient wastewater treatment.

2. MATERIALS AND METHODOLOGY

2.1 Chemicals

All analytical-grade reagents were procured from Star Scientific, Erode, and used without further purification. The chemicals employed in this study included aniline monomer (99.9%), ammonium persulfate (APS, 99.9%), hydrochloric acid (HCl, 37%), titanium tetraisopropoxide (TTIP, 97%), nitric acid (HNO_3, 65%), ethanol (99.9%), methanol (99.9%), and dimethylformamide (DMF, 99.9%), potassium hydroxide (KOH), methylene blue, malachite green, and Bismarck brown dyes.

2.2 Experiments

2.2.1 Synthesis of Polyaniline (PANI)

In a 250 mL beaker, aniline (4.65 g, freshly distilled) was dissolved in 1 M hydrochloric acid and cooled to 0–5 °C in an ice bath under continuous magnetic stirring. A pre-cooled solution of ammonium persulfate (11.4 g) in 1 M hydrochloric acid (50 mL) was added dropwise to the aniline solution, maintaining an aniline-to-oxidant molar ratio of 1:1. The reaction mixture gradually turned dark green, showing formation of polyaniline. The mixture was stirred for 5 h at 0–5 °C. The precipitate was collected by filtration, washed many times with deionized water and then with methanol until the filtrate was colorless, and dried to obtain polyaniline (Fig. 1).

2.2.2 Synthesis of TiO_2 Nanoparticles

In this work, titanium tetraisopropoxide (TTIP, 10 mL) was added dropwise into absolute ethanol (40 mL) under vigorous stirring at room temperature to obtain a clear solution. Separately, a mixture of distilled water (5 mL), ethanol (20 mL), and a few drops of nitric acid (to adjust pH to ~3–4) was prepared. This acidic aqueous solution was added dropwise to the TTIP–ethanol solution under continuous stirring, resulting in the formation of a white gel through hydrolysis and condensation reactions. The gel was aged for 1 day at room temperature, then dried at 80 °C to remove the solvent. The dried powder was washed with distilled water and absolute ethanol to remove residual organics, and finally calcined at 450–500 °C in air for 2–3 h to obtain crystalline anatase nano-TiO_2 (Kovačević *et al.* 2024).

2.2.3 Synthesis of Polymer Nanocomposites

A small quantity of polyaniline (PANI) was employed for nanocomposite fabrication. Approximately 250 mg of PANI was dispersed in 100 mL of dimethylformamide (DMF) within a 250 mL stoppered conical flask and subjected to continuous stirring followed by ultrasonication to obtain a uniform suspension. Owing to its limited solubility, the polymer remained finely distributed in the solvent after 48 h of agitation. Separately, TiO_2 nanoparticles were dispersed in acetone and ultrasonicated to improve particle distribution. The nanoparticle suspension was then introduced gradually into the PANI dispersion under continuous sonication. During the formation process, TiO_2 particles became embedded within the polymer framework, yielding PANI/TiO_2 nanocomposites. The resulting material was recovered by filtration, repeatedly rinsed with acetone to eliminate residual impurities, and subsequently dried for further characterization.

2.3 Characterization

UV–Vis spectroscopy (SHIMADZU), FTIR (BRUKER D8 Advance), and powder X-ray diffraction (Bruker) of the samples were recorded for structural characterization.

2.4 Photocatalytic Degradation Studies

Photocatalytic performance of polyaniline (PANI), TiO_2 nanoparticles, and PANI/TiO_2 nanocomposites was evaluated for BB, MG, and MB dyes under natural solar irradiation. Prior to light exposure, the catalyst–dye suspensions were magnetically stirred in the dark for 30 mins to reach adsorption–desorption equilibrium. Subsequently, mixtures were exposed to sunlight under continuous agitation. Stock dye solutions were prepared by dissolving 4 mg of each dye in 500 mL of deionized water. Various amounts of PANI, TiO_2, and PANI/TiO_2 photocatalysts were introduced into the dye solutions and subjected to solar illumination. The initial and residual dye concentrations were monitored using a double-beam UV–Vis spectrophotometer at characteristic absorption wavelengths of the respective dyes. Aliquots were collected at regular time intervals, and dye concentrations were determined from the absorbance measurements. The photocatalytic degradation efficiency R (%) was calculated by following the equation:

$$R(\%) = \frac{C_0 - C_t}{C_0} \quad \ldots (1)$$

where (C_0) shows the initial dye concentration before light irradiation, while (Ct) corresponds to the residual dye concentration measured after a specific irradiation period during the photocatalytic degradation process. All photocatalytic experiments were performed in triplicate, and the results were expressed as mean ± standard deviation. Statistical significance was evaluated using one-way ANOVA at $p < 0.05$. Experiments were

conducted in Chennai, India (13.08° N, 80.27° E), under clear-sky conditions between 10:00 a.m. and 3:00 p.m. The average solar intensity and reaction temperature were approximately 800 Wm^{-2} and 30–35 °C, respectively. The initial pH of the dye solutions was maintained at approximately 7.0. After irradiation, the catalyst was recovered by centrifugation at 6000 rpm for 10 min, washed with deionized water, and dried at 60 °C before further analysis. Similar enhancement in dye removal capability was reported for PANI/Mn-TiO_2 nanocomposites, where improved charge separation and reduced band-gap energy facilitated efficient methylene blue degradation (Poudel *et al.* 2020).

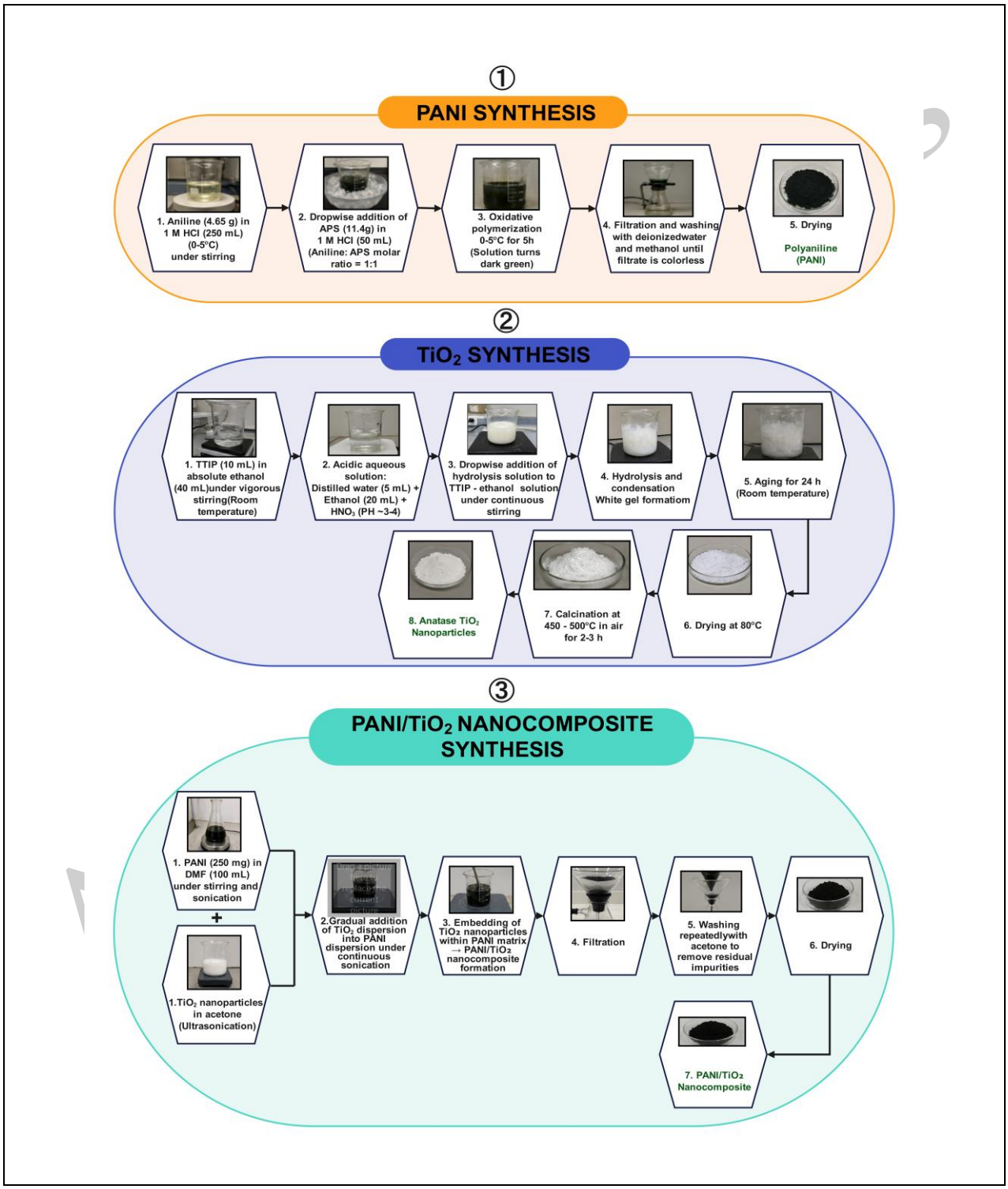

Fig. 1: Synthesis of polymer nanocomposites

3. RESULTS AND DISCUSSION

3.1 Photocatalyst Characterization

3.1.1 FTIR Spectral Characterization

Representative FTIR spectra of polyaniline (PANI), TiO_2 nanoparticles, and PANI/TiO_2 nanocomposites were presented in Figure 2(a–d). The broad absorption band observed in the 3424–3432 cm^{-1} region is attributed to overlapping N–H and O–H stretching vibrations. The characteristic absorption bands of PANI observed at 1574–1587 cm^{-1} and 1483–1492 cm^{-1} correspond to the stretching vibrations of quinoid and benzenoid ring structures of polyaniline, respectively. The absorption peaks located between 1286–1301 cm^{-1} are assigned to C–N stretching vibrations of aromatic amine groups. The bands observed in the 1225–1237 cm^{-1} and 1126–1138 cm^{-1} regions are attributed to the polaron structure and protonated PANI chains, confirming successful polymer formation. The TiO_2 nanoparticles exhibit characteristic Ti–O–Ti stretching vibrations in the 668–680 cm^{-1} region together with a strong Ti–O vibration appearing at 518–530 cm^{-1}. In addition, the TiO_2 spectrum displays a band at 1626–1634 cm^{-1}, which is associated with the bending vibration of surface hydroxyl groups and adsorbed water molecules. The simultaneous presence of the characteristic PANI and TiO_2 absorption bands in the nanocomposite spectra confirms successful addition of TiO_2 nanoparticles within the polyaniline matrix.

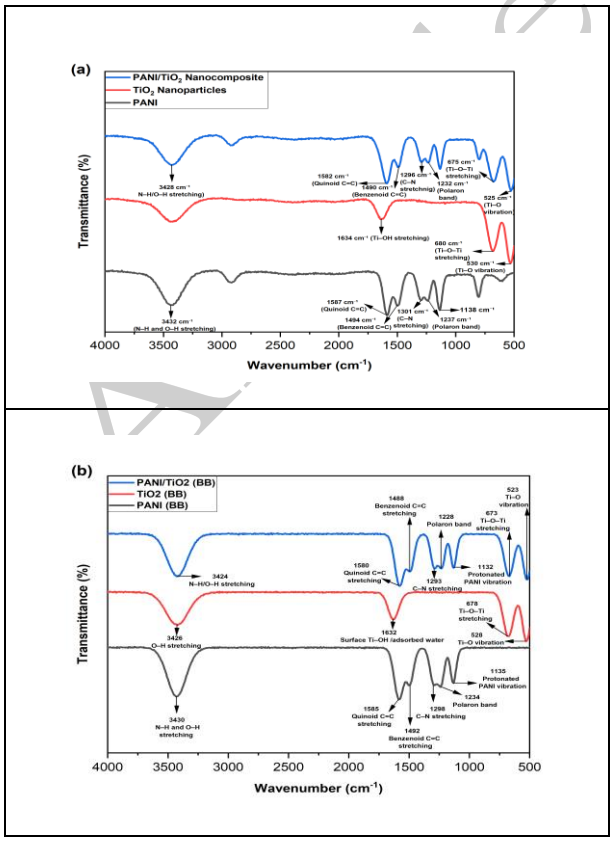

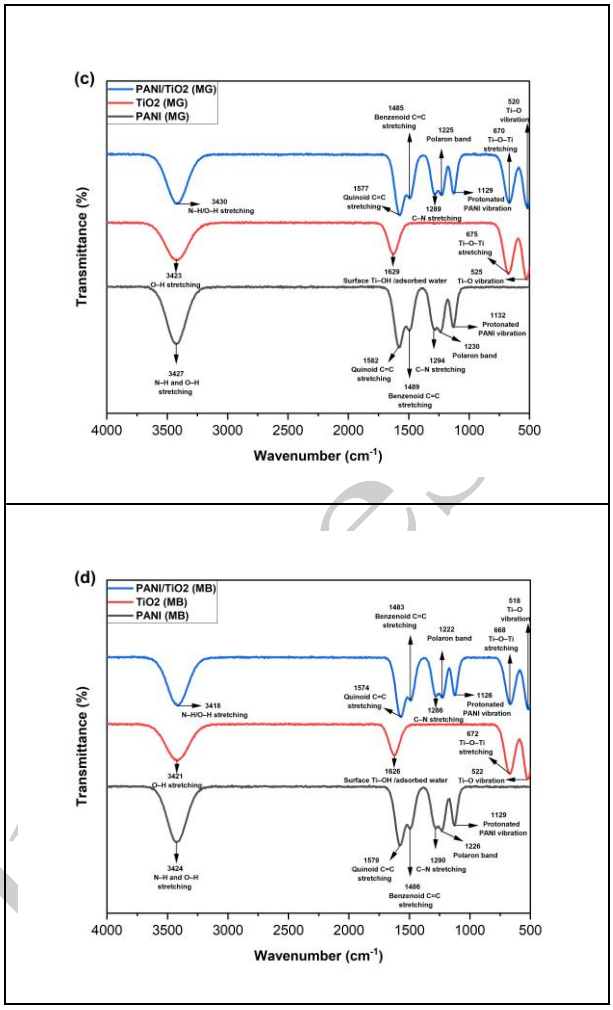

Fig. 2: FTIR spectra of PANI, TiO_2, and PANI/TiO_2 nanocomposite before and after photocatalytic degradation of Bismarck brown(BB), malachite green(MG) and methylene(MB) blue dyes

The nanocomposite spectrum shown in Fig. 2(a) exhibits the characteristic bands of both PANI and TiO_2. Slight shifts in band position and changes in peak intensity indicate interfacial interactions among polymer chains and TiO_2 nanoparticles, suggesting good compatibility and effective nanoparticle dispersion within the polymer matrix. In the PANI/TiO_2 nanocomposite, the characteristic PANI and TiO_2 bands exhibited red shifts of approximately 4–5 cm^{-1} compared with the pristine materials. These shifts and associated intensity changes indicate altered vibrational environments and interfacial interactions between PANI and TiO_2, confirming successful composite formation. These hydrogen-bonding and coordination interactions anchor TiO_2 within the PANI matrix, improve interfacial contact and nanoparticle dispersion, and may facilitate photogenerated charge transfer between PANI and TiO_2.The red shift of the N–H/O–H band from 3432 to 3428 cm^{-1} supports hydrogen bonding at the PANI–TiO_2 interface. These interactions improve interfacial adhesion and charge transfer, although FTIR alone cannot

conclusively distinguish hydrogen bonding from N–Ti coordination.

The FTIR spectra recorded after the photocatalytic process are presented in Figure 2(b-d). No significant changes in the positions of the characteristic PANI and TiO_2 absorption bands were observed, confirming the structural stability of the catalysts during photocatalysis. However, slight reductions in band intensity and minor spectral variations were detected, which are attributed to dye adsorption and surface reactions occurring during degradation. The PANI/TiO_2 nanocomposite exhibited more pronounced intensity changes than the individual components, indicating enhanced surface interaction with dye molecules and superior photocatalytic performance.

3.1.2 Ultraviolet–visible spectroscopy

Fig. 3a exhibited absorption bands at approximately 296–323 nm and 372–381 nm, corresponding to n–π* and π–π* electronic transitions within the conjugated polymer backbone. A distinct absorption peak was observed near 378–381 nm, characteristic of TiO_2 nanoparticles. This band was associated with electron excitation from the valence band to the conduction band under light irradiation. The absorption feature around 381 nm was detected in the nanocomposite samples but was absent in the pristine polymer matrix, confirming successful nanoparticle incorporation. These results suggest that the synthesized nanocomposites can be effectively activated under visible light or natural solar irradiation for photocatalytic applications. Previous studies reported that, g-C_3N_4/PANI-modified TiO_2 nanotube arrays exhibited enhanced visible-light absorption and superior photocatalytic activity, which was attributed to improved light harvesting and efficient separation of photogenerated charge carriers at the heterojunction interface (Zhou *et al.* 2020).

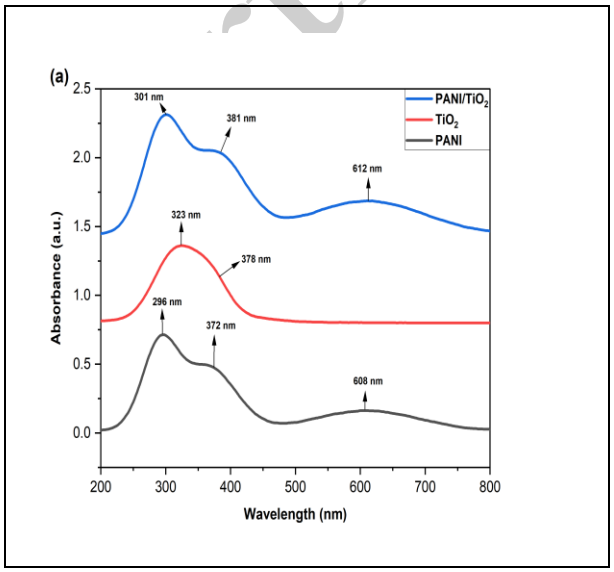

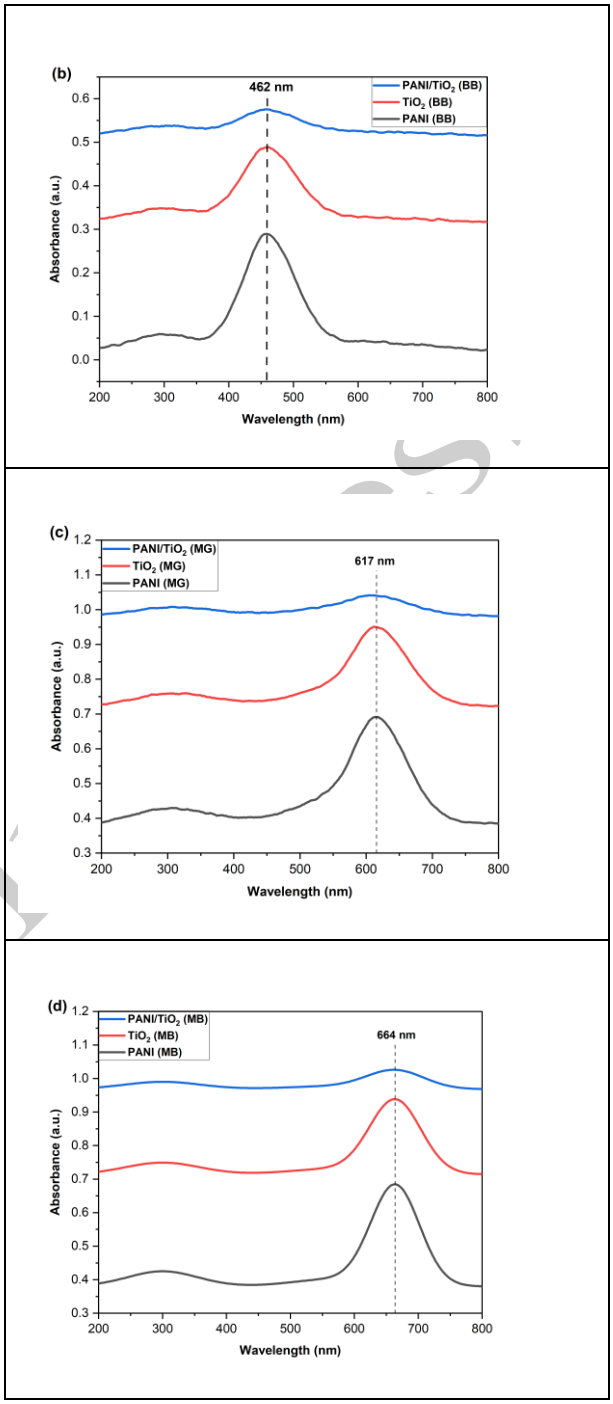

Fig. 3: UV–Visible absorption spectra of PANI, TiO_2, and PANI/TiO_2 nanocomposite before and after degradation of Bismarck brown(BB), malachite green(MG), and methylene blue(MB) dyes

Following the photocatalytic treatment, the UV–Vis spectra of the polymer matrix and nanocomposite samples were examined (Figure 3(b-d)). Absorption bands observed at approximately 462 nm (BB), 617 nm (MG), and 664 nm (M) in the nanocomposite samples were attributed to the residual color species of MG, BB, and MB dyes in the aqueous medium. In contrast, this absorption region was less

pronounced in the polymer matrix, indicating lower dye degradation efficiency. The reduced absorbance intensity in the nanocomposite system demonstrates its enhanced capability for the elimination of MG, BB, and MB dyes. Similar enhancement in visible-light absorption has been reported for PANI-coated semiconductor photocatalysts, where the conductive polymer promoted band-gap narrowing and prolonged charge-carrier lifetime, thereby improving photocatalytic efficiency (Zhang *et al.* 2020). Tauc plots of $(\alpha h\nu)^{1/2}$ versus $h\nu$were used to estimate the indirect optical band gaps of TiO_2 and $PANI/TiO_2$. The approximate optical band gap decreased from 3.28 eV for pristine TiO_2 to 2.03 eV for $PANI/TiO_2$, corresponding to an apparent reduction of 1.25 eV. This decrease indicates that PANI extends optical absorption into the visible region through its conjugated states and interfacial coupling with TiO_2.

3.1.3. XRD analysis

A broad diffraction halo centered around 2θ = 25.4° was observed for the PANI sample. The XRD patterns indicate the predominantly amorphous nature of the prepared materials. Generally, highly crystalline and structurally uniform materials produce sharp and intense diffraction peaks, whereas poorly ordered systems exhibit broad reflections. The presence of a wide halo in the 15.5–25.4° region further confirms the amorphous structure of the synthesized polymer. In previous studies, XRD analysis confirmed successful addition of PbS quantum dots into the PANI matrix, indicating effective composite formation. The diffraction peaks further verified the crystalline nature of the PbS phase within the composite (Chhabra *et al.* 2020).

As shown in Fig. 4, the diffraction peak around 2θ = 20.5° is associated with the spacing between aromatic ring planes in adjacent polymer chains, reflecting interchain packing characteristics. In addition, the prominent peak near 2θ = 25.4° can be attributed to interplanar spacing within the polymer network. The presence of these reflections suggests a certain degree of structural ordering and partial crystallinity in the synthesized material.

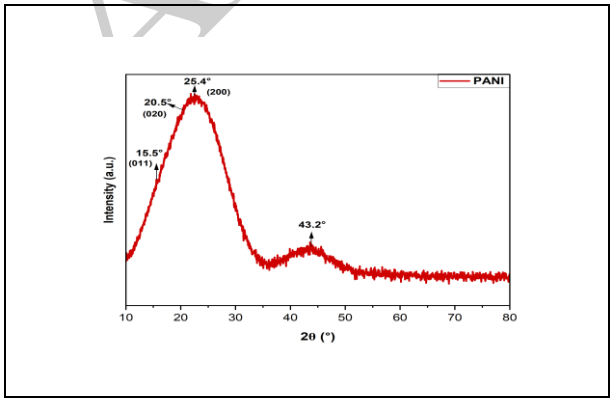

Fig. 4: XRD pattern of synthesized PANI polymer matrix

The peaks observed (Fig. 6) at 2θ values of 25.3°, 37.8°, 48.0°, 53.9°, 55.1°, 62.7°, 68.8°, 70.3°, and 75.0 ° correspond to the characteristic planes of crystalline TiO_2, confirming its well-defined crystal structure. The major reflections detected in the nanocomposite samples closely matched those of pure TiO_2, indicating that the crystal structure of the nanoparticles remained unchanged after incorporation into the polymer matrix. The TiO_2 reflections were indexed to the (101), (004), (200), (105), (211), (204), (116), (220), and (215) planes of tetragonal anatase TiO_2, consistent with JCPDS card No. 21-1272. The crystallite size was calculated using the Scherrer equation, $D = K\lambda/(\beta\cos\theta)$, and was found to be 10.2 nm for TiO_2 and 8.1 nm for $PANI/TiO_2$. The tetragonal lattice parameters calculated from the (200) and (004) reflections were approximately $a = 3.79$ Å $and\ c = c = 9.51$Å. After composite formation, the anatase peak positions remained nearly unchanged, while the reduced intensity and broadening of the peaks indicated the contribution of amorphous PANI and reduced coherent crystallinity without alteration of the TiO_2 phase. These findings confirm the successful dispersion and integration of TiO_2 nanoparticles within the composite system.

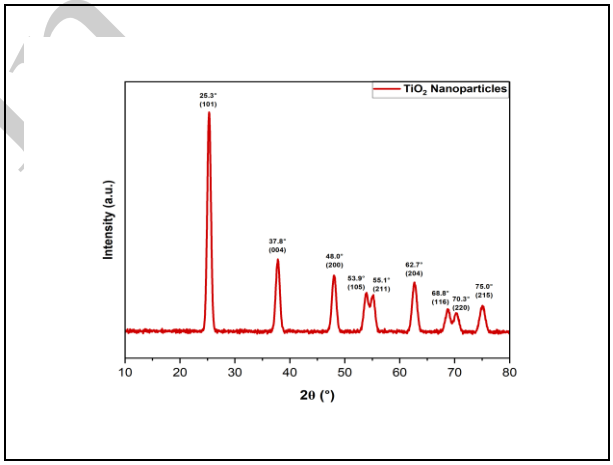

Fig. 5: XRD pattern of TiO_2 nanoparticles

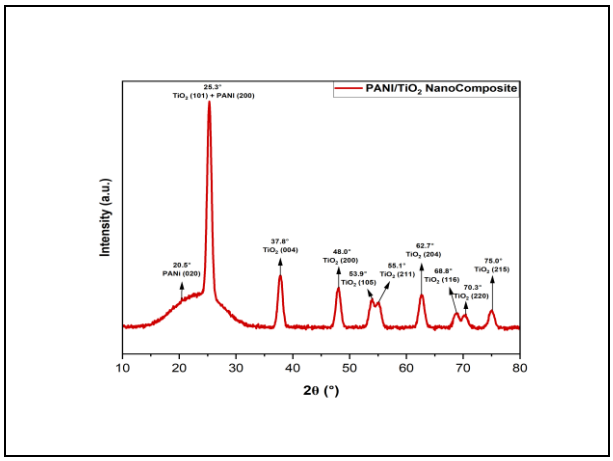

Fig. 6: XRD pattern of $PANI/TiO_2$ nanocomposite

3.1.4 Photocatalytic Performance of PANI, TiO_2 and PANI/TiO_2 Under Natural Sunlight

Photocatalytic degradation of MB, MG, and BB dyes under sunlight irradiation was evaluated using the polymer matrix, TiO_2 nanoparticles, and the nanocomposite catalyst. The effect of catalyst loading (100, 200, 300, 400, and 500 mg) on various irradiation periods (1–5 h) was investigated at a fixed dye concentration of 50 ppm, as illustrated in Figs. (7–21). The corresponding linear fitting coefficients were 0.949, 0. 979, and 0.963 for MB, MG, and BB, respectively, supporting the applicability of the pseudo-first-order kinetic model.

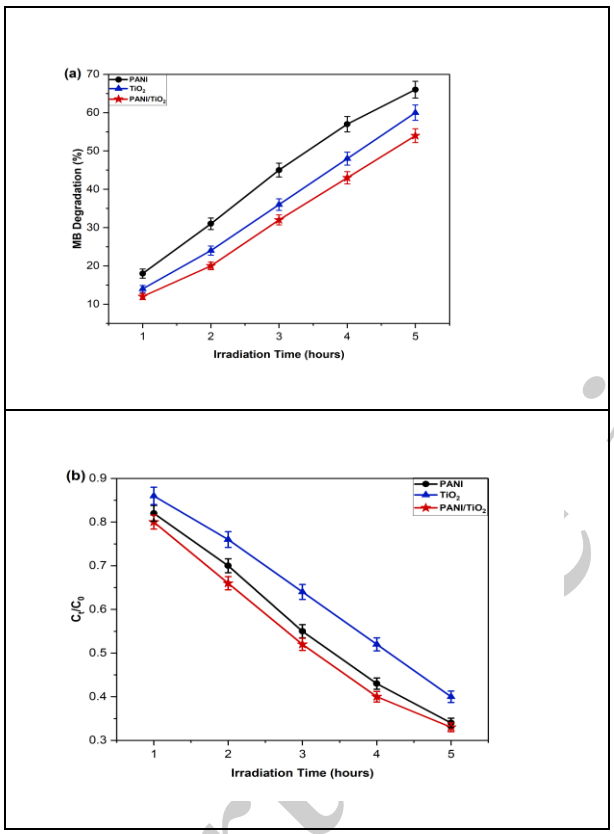

Fig. 7: Influence of 100 mg catalyst loading on MB dye degradation (a) and corresponding kinetic profiles and (b) under solar irradiation at 50 ppm concentration

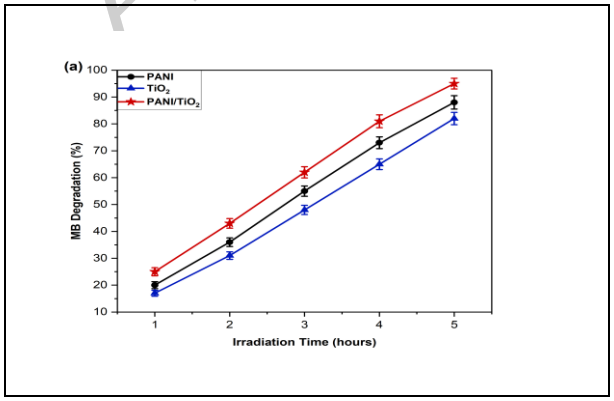

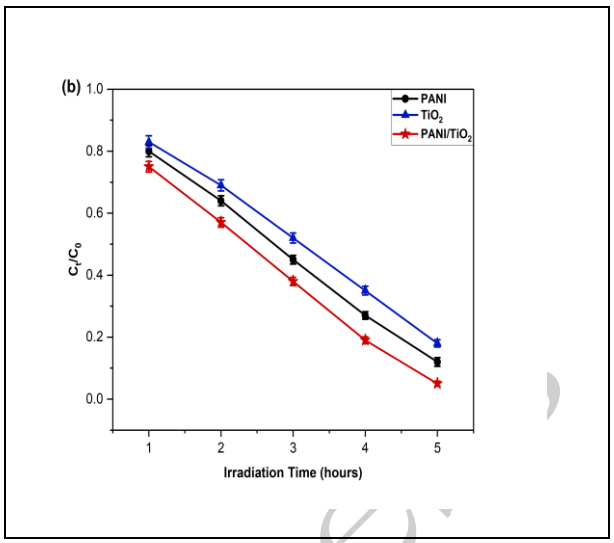

Fig. 8: Influence of 200 mg catalyst loading on MB dye degradation (a) and corresponding kinetic profiles and (b) under solar irradiation at 50 ppm concentration

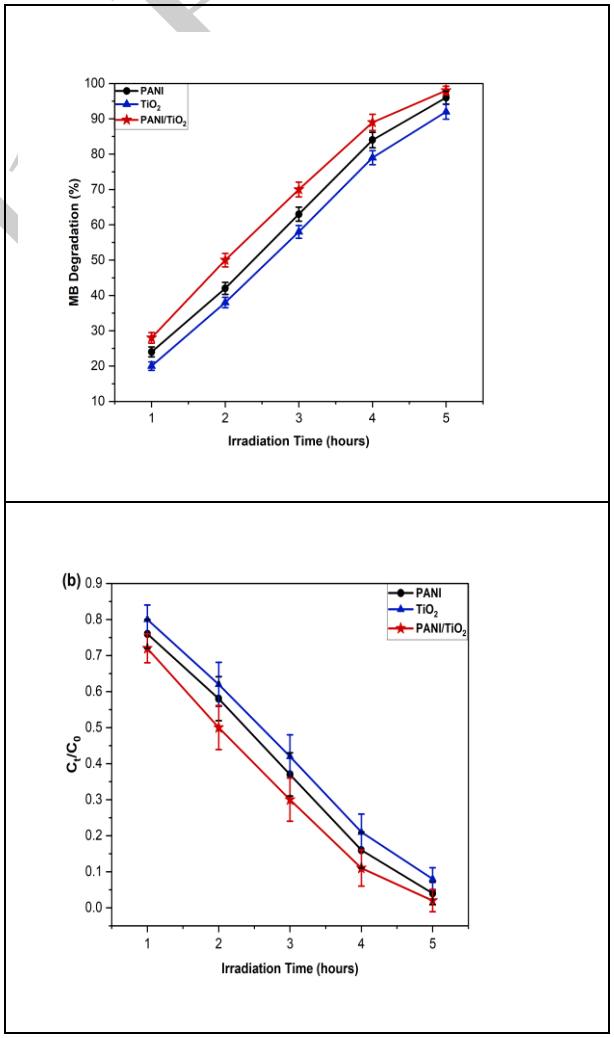

Fig. 9: Influence of 300 mg catalyst loading on MB dye degradation (a) and corresponding kinetic profiles (b) under solar irradiation at 50 ppm concentration

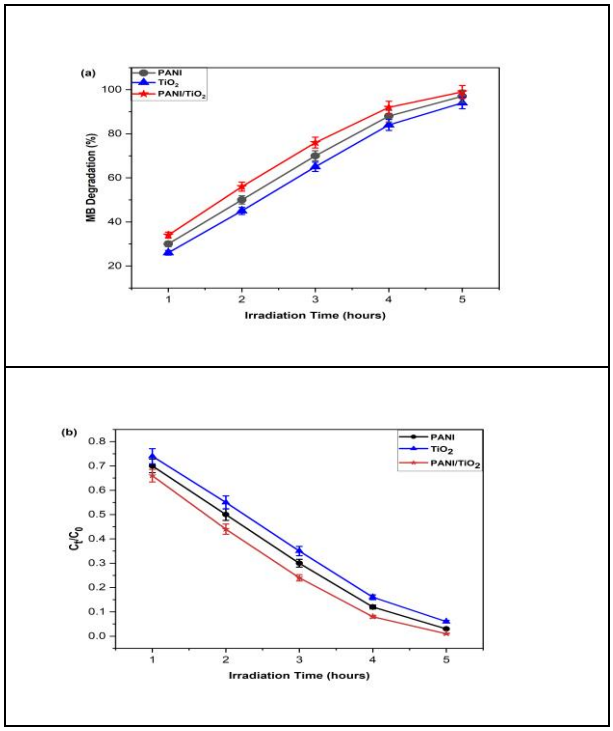

Fig. 10: Influence of 400 mg catalyst loading on MB dye degradation (a) and corresponding kinetic profiles (b) under solar irradiation at 50 ppm concentration

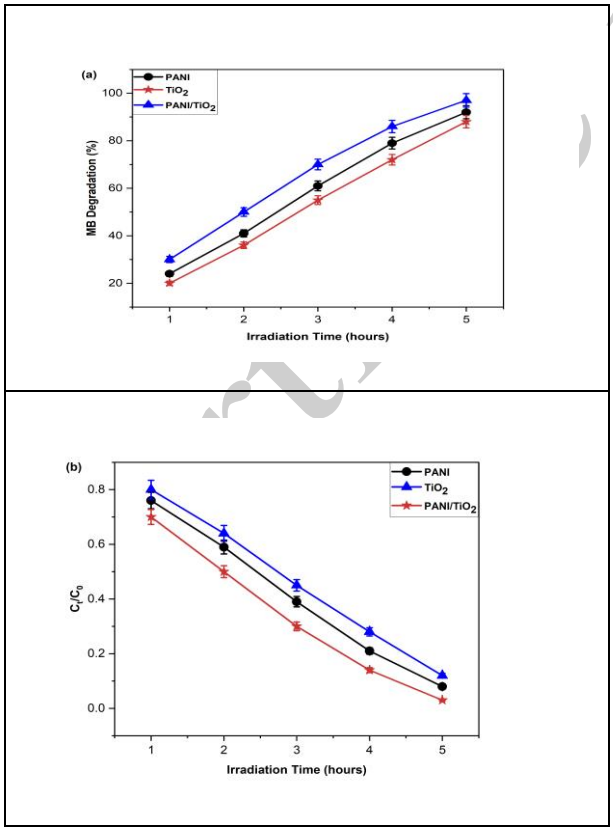

Fig. 11: Influence of 500 mg catalyst loading on MB dye degradation (a) and corresponding kinetic profiles (b) under solar irradiation at 50 ppm concentration

The degradation profiles of MB (Fig. 7–11), MG (Fig. 12–16), and BB (Fig. 17–21) under sunlight irradiation were presented as a function of exposure time. All measurements were performed in triplicate, and the error bars represent mean ± standard deviation. Statistical reproducibility was evaluated using one-way ANOVA at $p < 0.05$.

Results demonstrate progressive reduction of dye concentration with increasing irradiation duration. This confirms the effective photocatalytic performance of the prepared system. In previous studies, Ag_3PO_4/PANI@g-C_3N_4 nanocomposites achieved 99.6% degradation of monocrotophos due to enhanced electron–hole separation and efficient sunlight harvesting (Balasubramanian *et al.* 2020).

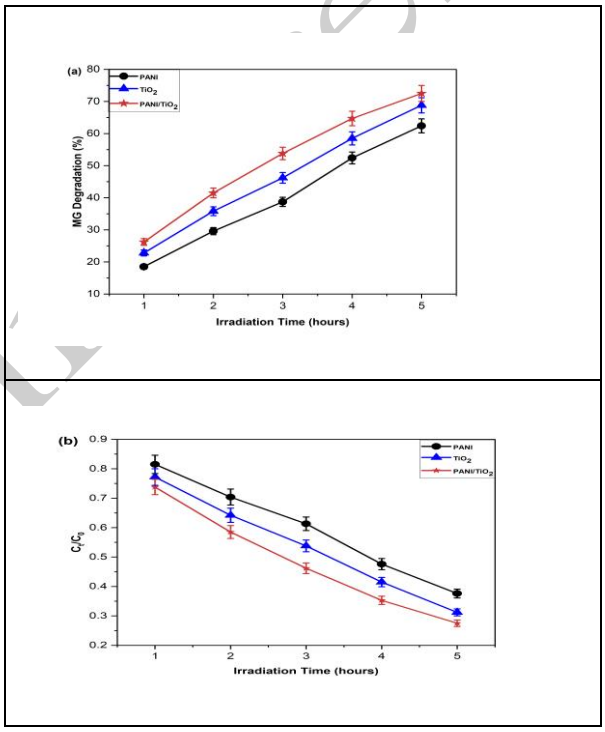

Fig. 12: Influence of 100 mg catalyst loading on MG dye degradation (a) corresponding kinetic profiles and (b) under solar irradiation at 50 ppm concentration

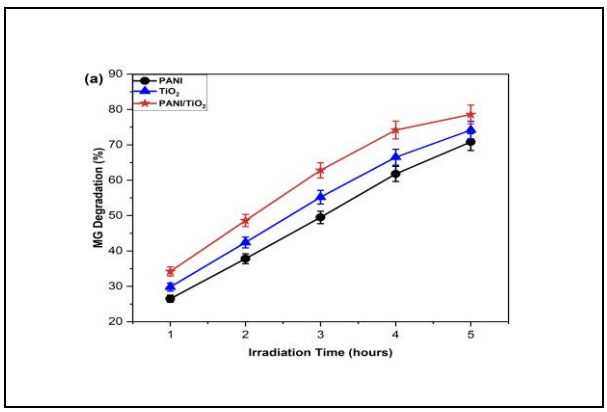

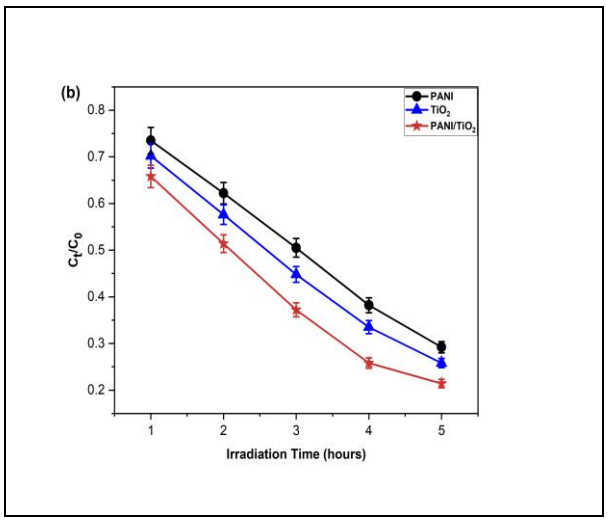

Fig. 13: Influence of 200 mg catalyst loading on MG dye degradation (a) corresponding kinetic profiles and (b) under solar irradiation at 50 ppm concentration

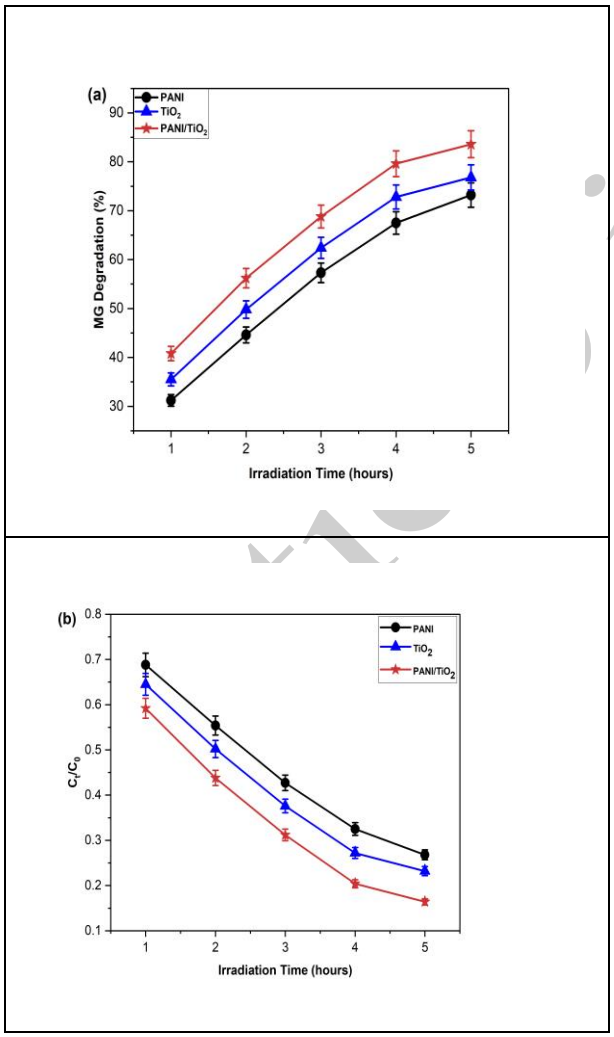

Fig. 14: Influence of catalyst loading (300 mg) on MG degradation performance (a) kinetic trends and (b) under solar irradiation at 50 ppm concentration

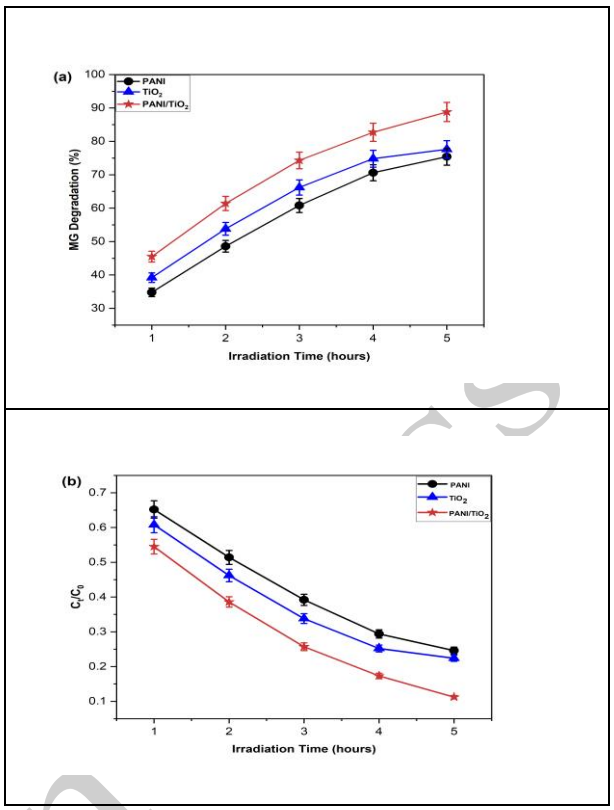

Fig. 15: Influence of 400 mg catalyst loading on MG dye degradation (a) corresponding kinetic profiles and (b) under solar irradiation at 50 ppm concentration

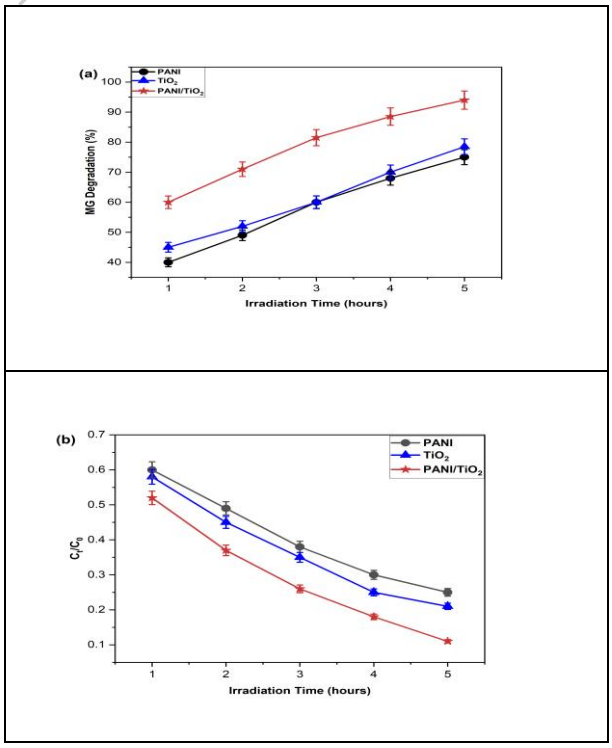

Fig. 16: Influence of catalyst dosage (500 mg) on MG degradation efficiency (a) kinetic response and (b) under solar irradiation at 50 ppm concentration

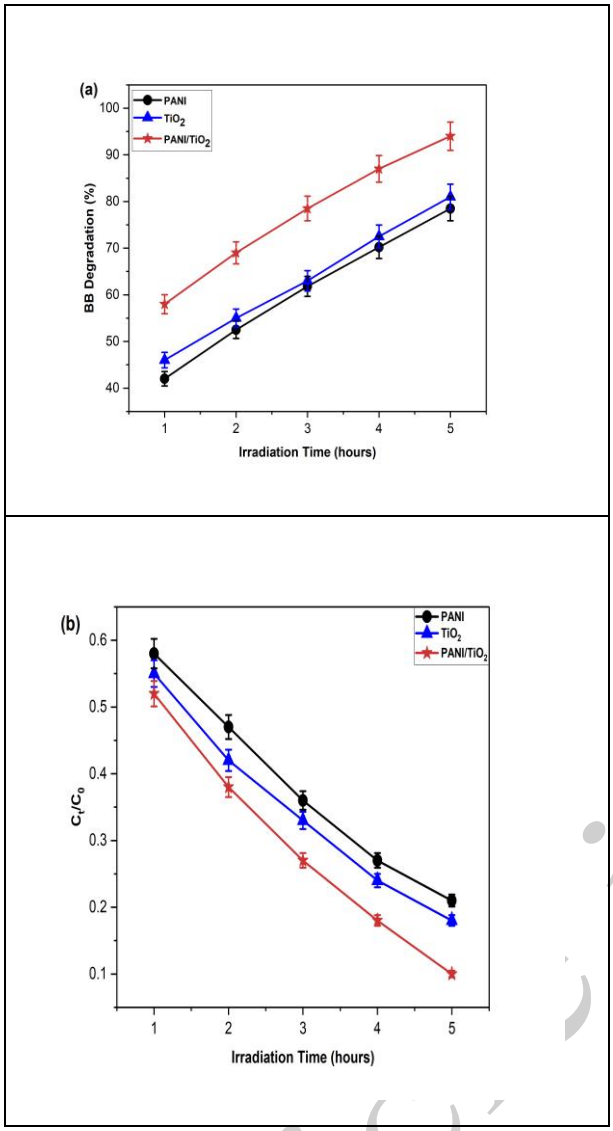

Fig. 17: Influence of catalyst dosage (100 mg) on BB degradation efficiency (a) kinetic response and (b) under solar irradiation at 50 ppm concentration

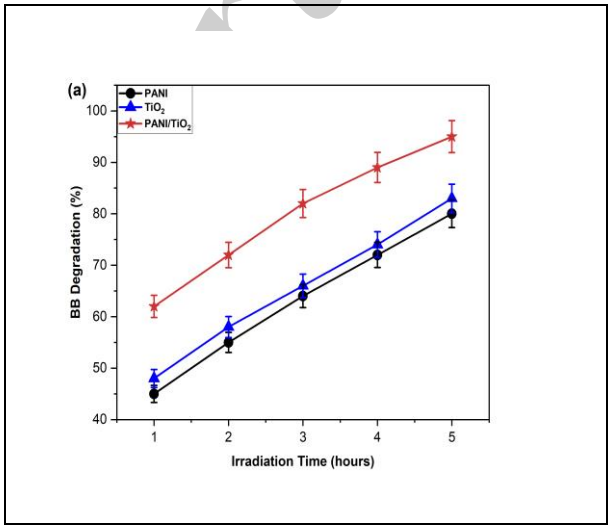

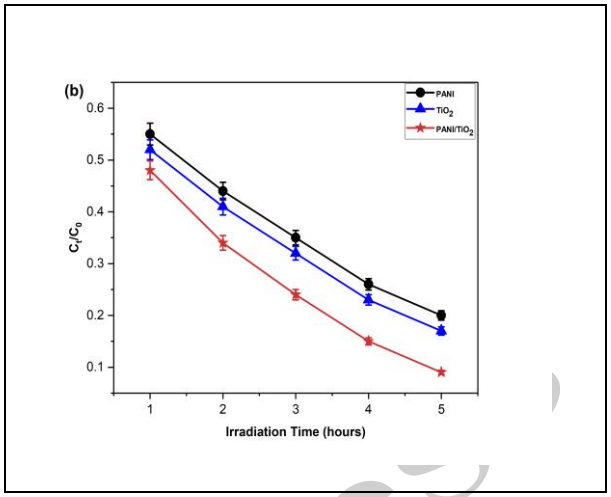

Fig. 18: Influence of 200 mg catalyst loading on BB dye removal (a) corresponding kinetic trends and (b) under solar irradiation at 50 ppm concentration

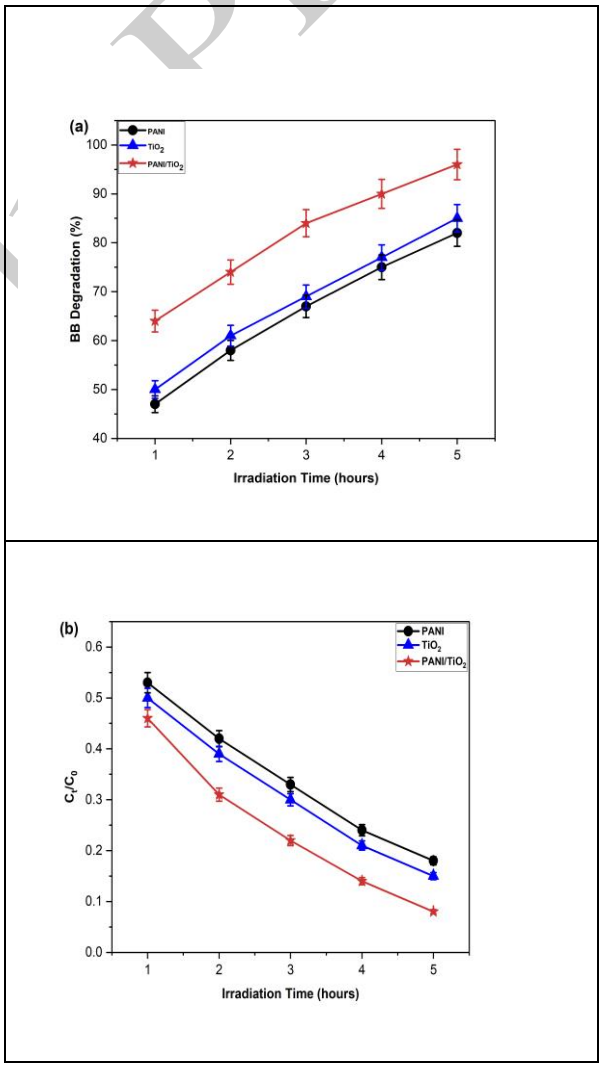

Fig. 19: Influence of 300 mg catalyst loading on MG dye degradation (a) corresponding kinetic profiles and (b) under solar irradiation at 50 ppm concentration

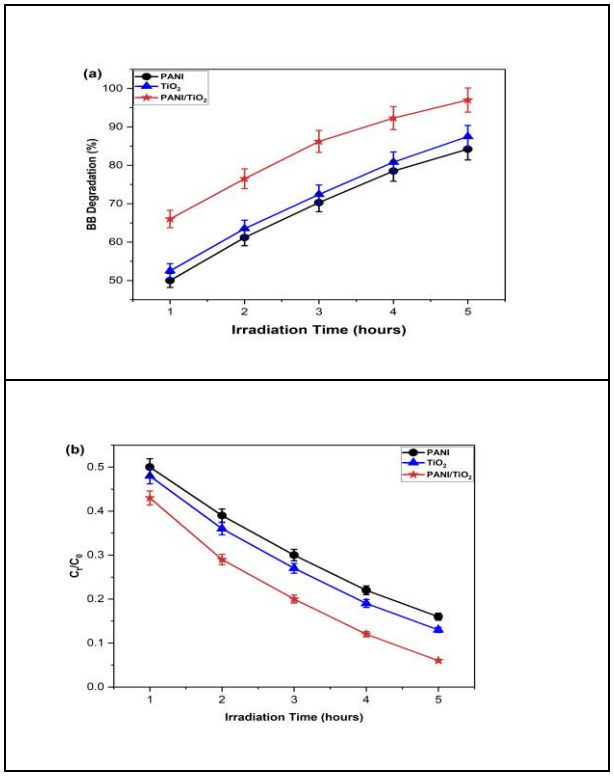

Fig. 20: Effect of 400 mg catalyst dosage on BB degradation efficiency: (a) kinetic behavior and (b) under solar irradiation at 50 ppm dye concentration

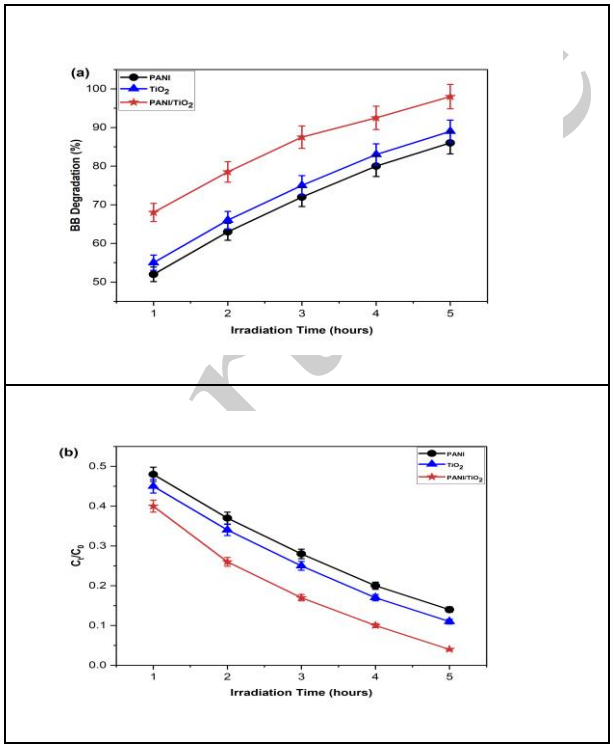

Fig. 21: Effect of 500 mg catalyst dosage on BB degradation efficiency (a) kinetic behavior and (b) under solar irradiation at 50 ppm dye concentration

The highest degradation efficiencies of MB (96%), MG (94%), and BB (98%) were achieved using 500 mg of the nanocomposite catalyst at a dye concentration of 50 ppm under natural sunlight irradiation for 5 h, as summarized in Table 1

Table 1. Dye degradation efficiency under optimum catalyst dosage (500 mg) and 50 ppm concentration

Dye	Degradation Efficiency (%)		
Catalyst	MB	MG	BB
PANI	85	75	75
$PANI/TiO_2$ (PNT)	96	94	98
TiO_2	89	78	83

The photocatalytic degradation rate constants for MB, MG, and BB were determined from the kinetic plots of Ct/C₀ versus irradiation time (Figs. 7–21). Degradation behavior was analyzed by following kinetic equation (2):

$$\ln = \frac{C_t}{C_0} = K_{\mathrm{App}} t \qquad \ldots (2)$$

The apparent rate constant (Kapp, min^{-1}) was evaluated using the pseudo-first-order kinetic model. The calculated rate constants for degradation of MB, MG, and BB were 0.2954 min^{-1}, 0.2876 min^{-1}, and 0.3815 min^{-1}, showing efficient photocatalytic degradation of the dye molecules.

3.2 Proposed Mechanism of Dye Photodegradation

Under light irradiation, electrons in the photocatalyst were excited from the valence to the conduction band, leading to the generation of electron–hole pairs. The photogenerated holes (h^+) participate in oxidation reactions, while excited electrons (e^-) were involved in reduction processes.

Conjugated polymers contain interconnected π-orbitals with delocalized electrons along their backbone, facilitating efficient charge transport and light absorption. Owing to these characteristics, several conducting polymers have been explored as visible-light-responsive photocatalysts. The extended π-conjugation enhances electron mobility and suppresses charge recombination, making these materials attractive for photocatalytic applications. Nevertheless, many polymer-based photocatalysts still exhibit moderate activity and often require UV–visible light irradiation for effective performance.

4. CONCLUSION

In this study, polyaniline (PANI), TiO_2 nanoparticles, and PANI/TiO_2 nanocomposites were successfully synthesized and characterized using UV–Vis, FTIR, and XRD analyses. Characterization outcomes confirmed successful incorporation of TiO_2 nanoparticles within the polymer matrix and revealed good interfacial compatibility among constituents. The synthesized nanocomposite exhibited improved optical absorption and favorable structural features for photocatalytic applications.

The photocatalytic performance of the prepared materials was evaluated through the degradation of MB, MG, and BB dyes under natural sunlight irradiation. Among the investigated photocatalysts, the PANI/TiO_2 nanocomposite showed higher activity, achieving degradation efficiencies of 96%, 94%, and 98% for MB, MG, and BB, at 50 ppm dye concentration using 500 mg catalyst within 5 h of irradiation. Degradation kinetics followed a pseudo-first-order model, with apparent rate constants of 0.2954 min^{-1}, 0.2876 min^{-1}, and 0.3815 min^{-1} for MB, MG, and BB.

The raised photocatalytic efficiency were attributed to synergistic interaction among conjugated polymer network and TiO_2 nanoparticles, which suppresses electron–hole recombination and facilitates efficient charge separation. These findings demonstrate the potential of PANI/TiO_2 for treating laboratory-prepared dye solutions under the tested conditions. The present study was limited to synthetic single-dye solutions, and mineralization, catalyst recyclability, and performance in real wastewater were not evaluated. Future work should investigate TOC/COD mineralization, catalyst stability and reuse, possible Ti leaching, real industrial wastewater, and large-scale solar photocatalytic applications.

FUNDING

This research received no specific grant from any funding agency in the public, commercial, or not-for-profit sectors.

CONFLICTS OF INTEREST

The authors declare that there is no conflict of interest.

COPYRIGHT

REFERENCES

Abedin, M. M., Zaman, S. K. M., Mondal, A., Sultana, M., Amena, M. R., Hossain, M. S., Durjoy, M. N. R., Chakraborty, A. K., Rahman, M. M., Rahaman, M. H., Khatun, M. A. and Nur, A. S. M., Strategic nitrogen doping of Ca-TiO_2 photocatalyst for improved dye degradation under UV–Vis irradiation, *Appl. Catal. O: Open*, 213, 207095(2026). https://doi.org/10.1016/j.apcato.2026.207095

Ahmadiasl, R., Moussavi, G., Shekoohiyan, S. and Razavian, F., Synthesis of Cu-Doped TiO_2 Nanocatalyst for the Enhanced Photocatalytic Degradation and Mineralization of Gabapentin under UVA/LED Irradiation: Characterization and Photocatalytic Activity, *Catal.*, 12(11), 1310(2022). https://doi.org/10.3390/catal12111310

Alwared, A. I., Mohammed, N. A., Al-Musawi, T. J. and Mohammed, A. A., Solar-Induced Photocatalytic Degradation of Reactive Red and Turquoise Dyes Using a Titanium Oxide/Xanthan Gum Composite, *Sustain.*, 15(14), 10815(2023). https://doi.org/10.3390/su151410815

Balasubramanian, J., Ponnaiah, S. K., Periakaruppan, P. and Kamaraj, D., Accelerated photodeterioration of class I toxic monocrotophos in the presence of one-pot constructed Ag_3PO_4/polyaniline@g-C_3N_4 nanocomposite: efficacy in light harvesting, *Environ. Sci. Pollut. Res.*, 27(2), 2328–2339(2020). https://doi.org/10.1007/s11356-019-06811-6

Chen, D. D., Yi, X. H., Ling, L., Wang, C. C. and Wang, P., Photocatalytic Cr (VI) sequestration and photo-Fenton bisphenol A decomposition over white light responsive PANI/MIL-88A(Fe), *Appl. Organomet. Chem.*, 34(9), e5795(2020). https://doi.org/10.1002/aoc.5795

Chinnusamy. C. Thiyagarajan R, Investigation of $BaZrO_3$ Nanoparticles for Photocatalytic Activity and the Effects of Y-doping, *J. Environ. Nanotechnol.,* 13 (3) 456-466 (2024). https://doi.org/10.13074/jent.2024.09.243849

Chhabra, V. A., Kaur, R., Walia, M. S., Kim, K. H. and Deep, A., PANI/PbS QD nanocomposite structure for visible light driven photocatalytic degradation of rhodamine 6G, *Environ. Res.*, 186, 109615(2020). https://doi.org/10.1016/j.envres.2020.109615

Chkirida, S., Zari, N., Achour, R., Qaiss, A. E. K. and Bouhfid, R., Effect of iron doped titanium oxide encapsulated in alginate on photocatalytic activity for the removal of dye pollutants, *RSC Adv.*, 10(38), 22311–22317 (2020). https://doi.org/10.1039/d0ra02898c

Gaddala, B., Devi, K. V, Balakrishnan, V., Sundramurthy, V. P., Hariprabhu, M., Mayakannan, S., Kadaikunnan,

S. and Khaled, J. M., Evaluation of detoxification performance of Pithecellobium dulce seed pod powder upon acid treatment: removal of reactive red 195-A dye and kinetic analysis, *Zeitschrift Fur Physikalische Chemie*, 239(6), 885–910 (2025). https://doi.org/10.1515/zpch-2024-0879

Gholizadeh, F., Dianat, M. J. and Izadbakhsh, A., Photocatalytic degradation of phenol using silica SBA-16 supported TiO_2, *React. Kinetics, Mech. Catal.*, 130(2), 1171–1192 (2020). https://doi.org/10.1007/s11144-020-01817-5

Gunti, S., Alamro, T., McCrory, M. and Ram, M. K., The use of conducting polymer to stabilize the nanostructured photocatalyst for water remediation, *J. Environ. Chem. Eng.*, 5(6), 5547–5555 (2017). https://doi.org/10.1016/j.jece.2017.10.036

Hasan, J., Li, H., Tian, G. and Qin, C., Fabrication of Cr_2S_3-GO-TiO_2 composite with high visible-light-driven photocatalytic activity on degradation of organic dyes, *Chem. Phy.*, 539, 110950(2020). https://doi.org/10.1016/j.chemphys.2020.110950

Hassan, F., Bonnet, P., Dangwang Dikdim, J. M., Gatcha Bandjoun, N., Caperaa, C., Dalhatou, S., Kane, A. and Zeghioud, H., Synthesis and Investigation of TiO_2/g-C_3N_4 Performance for Photocatalytic Degradation of Bromophenol Blue and Eriochrome Black T: Experimental Design Optimization and Reactive Oxygen Species Contribution, *Water (Switzerland)*, 14(20), 3331(2022). https://doi.org/10.3390/w14203331

Hema. K, Anishia. S. R., Rajeswari. S, Padmavathy V. Sujatha. S, Thiyagu M., Green Synthesis and Multifunctional Applications of Moringa Oleifera-enhanced TiO_2 Nanocomposites, *J. Environ. Nanotechnol.,* 14 (1) 7-17 (2025) https://doi.org/10.13074/jent.2025.03.2511225

Hiremath, A., Pattar, J., Chandra, S. S., Rao, H. N. A., Sreekanth, R., Mahendra, K., Manohara, S. and Aravinda, T., Designing PANI/g-C_3N_4/Cr_2O_3 composites for integrated environmental and dielectric functionalities, *Surf. Interf.*, 72, 107177(2025). https://doi.org/10.1016/j.surfin.2025.107177

Idriss, H., Ibrahem, M. A. and Modwi, A. Photocatalytic degradation of Congo red pigment by V_2O_5-TiO_2 nanohybrid, *Zeitschrift Fur Naturforschung - Section J. Phy. Sci.*, 78(1), 67–76 (2023). https://doi.org/10.1515/zna-2022-0166

Jebasingh, J. A., Vidyavathy, S. M. and Stanley, R., Ultra-fast degradation of thiazine dyes in the presence of natural sunlight by coupling of titania with zinc oxide nanoparticles in the room temperature, *J. Iran. Chem. Soc.*, 21(4), 1131–1140 (2024). https://doi.org/10.1007/s13738-024-02984-1

Kisała, J., Gnilitskyi, I., Cieniek, B., Krzemiński, P., Marchewka, M., Barylyak, A. and Bobitski, Y., Synthesis of micro-spikes and herringbones structures by femtosecond laser pulses on a titanium plate—a new material for water organic pollutants degradation, *Mater.*, 14(19), 5556(2021). https://doi.org/10.3390/ma14195556

Koe, W. S., Chong, W. C., Pang, Y. L., Koo, C. H., Ebrahim, M. and Mohammad, A. W., Novel nitrogen and sulphur co-doped carbon quantum dots/titanium oxide photocatalytic membrane for in-situ degradation and removal of pharmaceutical compound, *J. Water Process Eng*., 33, 101068(2020). https://doi.org/10.1016/j.jwpe.2019.101068

Kovačević, A., Radoičić, M., Marković, D., Šaponjić, Z. and Radetić, M., Recycled Jute Non-Woven Material Coated with Polyaniline/TiO_2 Nanocomposite for Removal of Heavy Metal Ions from Water, *Mol.*, 29(18), 4366(2024). https://doi.org/10.3390/molecules29184366

Loganathan, A., Sethupathi, N., Mahalingam, P. and Sivakumar, P., Green Synthesis, Structural Characterization and Kinetics of Photocatalytic Degradation of Reactive Blue 19 Dye Using CeO_2-doped Reduced Graphene Oxide Nanohybrid, *J. Environ. Nanotechnol.*, 15(1), 576–585(2026). https://doi.org/10.13074/jent.2026.03.2612126

Patidar, M., Sharma, D., Devi, G. M., Sujithra, L. R., Kumar, S. S. and Kandavalli, S. R., Enhanced Adsorptive Removal of Methylene Blue Using Kaolinite–$MnFe_2O_4$ Nanocomposites: Synthesis, Characterization and Adsorption Mechanisms, *J. Environ. Nanotechnol.*, 15(1), 405–417 (2026). https://doi.org/10.13074/jent.2026.03.2541911

Poudel, M. B., Yu, C. and Kim, H. J., Synthesis of conducting bifunctional polyaniline@mn-TiO_2 nanocomposites for supercapacitor electrode and visible light driven photocatalysis, *Catal.*, 10(5), 546 (2020). https://doi.org/10.3390/catal10050546

Rao, D. P., Krishnasamy, V. D., Selvaraju, M., Sundramurthy, V. P., Kandavalli, S. R., Chitra, M. S., Sivasamy, N. and Thirumoorthy, P., Adsorptive removal of cadmium from electroplating wastewater using hybrid composite of thiol-grafted seed gum of Tamarindus indica and Teff hay biocarbon, *Zeitschrift Fur Physikalische Chemie*, 239(5), 633–654 (2025). https://doi.org/10.1515/zpch-2024-0715

Rigoti, E., Schwanke, A. J., Araújo, K. C. F., Martínez-Huitle, C. A. and Pergher, S. B. C., Titanium oxide supported on montmorillonite clays for environmental applications, *J. Mex. Chem. Soc.*, 63(3), 1–12 (2019). https://doi.org/10.29356/jmcs.v63i3.708

Saha, S., Chaudhary, N., Kumar, A. and Khanuja, M., Polymeric nanostructures for photocatalytic dye degradation: polyaniline for photocatalysis, *SN Appl. Sci.*, 2(6), 1115(2020). https://doi.org/10.1007/s42452-020-2928-4

Usman, M., Adnan, M., Ali, S., Javed, S. and Aftab Akram, M., Preparation and characterization of pani@nio visible light photocatalyst for wastewater

treatment, *Chem, Select*, 5(40), 12618–12623(2020). https://doi.org/10.1002/slct.202003540

Vivek, P., Balu, S. and Sundramoorthy, A. K., Photocatalytic Degradation of Binary Dyes, Methyl Orange and Methyl Green, in Aqueous Media Using 2D g-C_3N_4/Polyaniline/Silver Nanocomposite. *Curr. Nanosci.*, 22(1), 154–168(2026). https://doi.org/10.2174/0115734137356016250211063405

Wang, Y., Zhang, P., Zhang, T. C., Xiang, G., Wang, X., Pehkonen, S. and Yuan, S., A magnetic γ-Fe_2O_3@PANI@TiO_2core-shell nanocomposite for arsenic removalviaa coupled visible-light-induced photocatalytic oxidation-adsorption process, *Nanoscale Adv.*, 2(5), 2018–2024 (2020). https://doi.org/10.1039/d0na00171f

Weldekirstos, H. D., Girma, P., Tedla, A., Aberra, N. and Negash, A., Facile Synthesis and Characterization of TiO_2/NiO Composite for Photocatalytic Removal of Organic Pollutant Under Sunlight Irradiation, *Water, Air Soil Pollut.*, 236(9), 580(2025). https://doi.org/10.1007/s11270-025-08217-2

Zhang, F., Li, X., Zhao, Q., Chen, G. and Zhang, Q., High-performance In_2O_3@PANI core@shell architectures with ultralong charge carriers lifetime for photocatalytic degradation of gaseous 1,2-dichlorobenzene, *Appl. Catal. B: Environ.*, 263, 118278(2020). https://doi.org/10.1016/j.apcatb.2019.118278

Zhou, Q., Zhao, D., Sun, Y., Sheng, X., Zhao, J., Guo, J. and Zhou, B., g–C_3N_4– and polyaniline-co-modified TiO_2 nanotube arrays for significantly enhanced photocatalytic degradation of tetrabromobisphenol A under visible light, *Chemosph.*, 252, 126468(2020). https://doi.org/10.1016/j.chemosphere.2020.126468